ELSEVIER

International Journal of Heat and Fluid Flow 22 (2001) 573–582

International Journal of HEAT AND FLUID FLOW

www.elsevier.com/locate/ijhff

Isolating curvature effects in computing wall-bounded turbulent flows

Christopher L. Rumsey *, Thomas B. Gatski, W. Kyle Anderson [1], Eric J. Nielsen

Computational Modeling and Simulation Branch, NASA Langley Research Center, Mail Stop 128, Hampton, VA 23681-2199, USA

Received 5 April 2001; accepted 10 June 2001

Abstract

An adjoint optimization method is utilized to design an inviscid outer wall shape required for a turbulent flow field solution of the So–Mellor convex curved wall experiment using the Navier–Stokes equations. The associated cost function is the desired pressure distribution on the inner wall. Using this optimized wall shape with a Navier–Stokes method, the abilities of various turbulence models to simulate the effects of curvature without the complicating factor of streamwise pressure gradient are evaluated. The one-equation Spalart–Allmaras (SA) turbulence model overpredicts eddy viscosity, and its boundary layer profiles are too full. A curvature-corrected version of this model improves results, which are sensitive to the choice of a particular constant. An explicit algebraic stress model does a reasonable job predicting this flow field. However, results can be slightly improved by modifying the assumption on anisotropy equilibrium in the model's derivation. The resulting curvature-corrected explicit algebraic stress model (EASM) possesses no heuristic functions or additional constants. It slightly lowers the computed skin friction coefficient and the turbulent stress levels for this case, in better agreement with experiment. The effect on computed velocity profiles is minimal.

Keywords: Streamline curvature; Turbulence models; Zero pressure gradient; Design optimization; Explicit algebraic stress

1. Introduction

It has long been recognized that many turbulence models in use today are incapable of producing correct physical behavior near curved surfaces. Much of this information comes from the use of boundary layer codes (e.g., see Wilcox, 1998) applied to curved flows with near-zero pressure gradient (e.g., So and Mellor, 1973; Gillis and Johnston, 1983). The few applications of Navier–Stokes codes to curved wall-bounded flows have generally been for cases with substantial pressure gradients, such as the U-duct test case of Monson and Seegmiller (1992). The use of a test case with pressure gradient can complicate the analysis by making it difficult to isolate the effects of curvature from the effects of pressure gradient. Also, in the Monson and Seegmiller case for example, one must contend with boundary layer separation and consequently a loss of two-dimensionality.

Even though experiments such as So and Mellor and Gillis and Johnston are excellent validation cases for turbulence model evaluation because they isolate the effects of curvature on flow field dynamics, their usefulness has been restricted to boundary layer solution methodologies. This restriction is due to the fact that in these experiments the outer wall shape has not been explicitly documented. The only information recorded is that the outer wall was manually adjusted during the experiment to yield the desired (near-zero) pressure gradient along the inner curved wall. Additionally, in the case of So and Mellor, a local tangential jet was used at the outer wall near the start of the curve to maintain attached flow on this wall; while in the case of Gillis and Johnston, local boundary layer bleeding accomplished the same thing. From the standpoint of boundary layer methods, this information is adequate. However, these issues produce a significant challenge for the modeling of the entire two-wall setup, as is required in a Navier–Stokes simulation, and preclude this type of experimental data from being more fully utilized.

Today, with advances made in optimization methods in CFD, it is now possible to find an outer wall shape that yields a specified pressure distribution on the inner wall. As a result, Navier–Stokes simulations can be relatively easily accomplished on test cases for which boundary layer codes were the only viable option in the past.

In previous work (Rumsey et al., 2000), three turbulence models were used to investigate the U-duct flow of Monson and Seegmiller. The three models employed were the one-equation Spalart–Allmaras (SA) (Spalart and Allmaras, 1994), two-equation Menter shear stress transport (SST) (Menter, 1994), and two-equation explicit algebraic stress model (EASM) (Rumsey et al., 2000), which is based on the work of

* Corresponding author. Tel.: 757-864-2165; fax: 757-864-8816.
E-mail address: c.l.rumsey@larc.nasa.gov (C.L. Rumsey).
[1] Currently at Symantec Corporation.

0142-727X/01/$ - see front matter
PII: S0142-727X(01)00122-9

Notations

a_{ref}	reference speed of sound
a_i, C_i, C_1^0, C_1^1	pressure–strain model constants
b_{ij}	anisotropy tensor
c_{b1}	constant in SA model
c_{f}	skin friction coefficient, $\tau_{\text{w}}/\frac{1}{2}\rho u_{\text{ref}}^2$
c_{p}	surface pressure coefficient, $(p-p_{\text{ref}})/\frac{1}{2}\rho u_{\text{ref}}^2$
c_{r1}, c_{r2}, c_{r3}	constants in SARC model
$C_{\varepsilon 1}$, $C_{\varepsilon 2}$	constants in ε-equation
D	flow parameter, $[\frac{1}{2}(S^2+W^2)]^{1/2}$
d	normal distance from the wall
f_{r1}	rotation/curvature correction function in SARC model, Eq. (15)
f_{t2}	function in SA model
g	function in EASM, Eq. (4)
K	turbulent kinetic energy
M	Mach number, $u_{\text{ref}}/a_{\text{ref}}$
P	part of production term in SA model
P'	part of production term in SARC model
$\mathscr{P}$	K production term
p	pressure
R	radius of curvature
$\mathscr{R}^2$	flow parameter, Eq. (14)
r^*	flow parameter, S/W
$\tilde{r}$	flow parameter in SARC model, Eqs. (16), (17)
S_{ij}	kinematic strain rate tensor, $(\partial u_i/\partial x_j+\partial u_j/\partial x_i)/2$
S	scalar measure of strain, $(2S_{ij}S_{ij})^{1/2}$
s	length measured along inner wall
t	time
u^+	wall variable, u/v^*
u, v	velocities parallel and normal to inner wall
u_{ref}	inlet (reference) velocity
$\overline{u'u'}$, $\overline{v'v'}$	turbulent normal stresses, Eqs. (19), (20)
$\overline{u'v'}$	turbulent shear stress, Eq. (18)
v^*	wall-friction velocity, $(\tau_{\text{w}}/\rho)^{1/2}$
W_{ij}	rotation rate tensor, $(\partial u_i/\partial x_j-\partial u_j/\partial x_i)/2$
W_{ij}^*	"effective" rotation rate tensor in EASMCC, $W_{ij}-\Omega_{ij}/a_2$
W	scalar measure of rotation, $(2W_{ij}W_{ij})^{1/2}$
x, y	Cartesian coordinates
y^+	wall variable, $\mathrm{d}v^*/v$

Greeks

α	strain-rate tensor principal axes angle
δ	boundary layer thickness
δ_{ij}	Kronecker delta
ε	dissipation rate of K
ϵ_{ijk}	alternating tensor, $(i-j)(j-k)(k-i)/2$
$\gamma_0, \gamma_1, \gamma_0^*, \gamma_1^*$	parameters in EASM, Eqs. (5), (6)
τ_{ij}	turbulent stress tensor
τ_{w}	wall shear stress
v	kinematic viscosity
$\tilde{v}$	modified eddy viscosity term in SA model
Θ	body tangent vector angle
Ω_{ij}	transformation tensor, Eq. (10)
ω_m	components of system rotation rate vector

Gatski and Speziale (1993). All models behaved similarly in the curved region, and all failed to predict the suppression of the turbulent shear stress caused by the convex curvature. Overall, the EASM was judged to be superior to the other two models for this flow field. However, as mentioned above, it is difficult to isolate the effects of curvature from other effects in the Monson and Seegmiller case.

In the present study, we model the So–Mellor case, which removes the complications of pressure gradient and boundary layer separation from consideration. Two of the above turbulence models (SA and EASM) are employed. Both of these turbulence models include recently developed curvature corrections, and can be run both with and without the corrections in place. We first describe an optimization method used to determine the outer wall shape, given the So–Mellor experimental inner wall pressure distribution. We then apply a Navier–Stokes code to the case. We attempt to answer the following questions regarding the isolated effect of curvature in zero pressure gradient flow:

1. how well do existing models *without* curvature correction handle convexly curved wall-bounded flow?
2. what aspects of the flow are missed, and how significant are the missed effects?
3. how much improvement is gained by employing curvature correction terms to the turbulence models?

2. The optimization method

In the fully discrete adjoint approach for design optimization, described in Nielsen and Anderson (2001), Anderson and Bonhaus (1999), and Nielsen and Anderson (1999), a cost function is defined and augmented with the flow equations as constraints. The approach is used in an unstructured-grid framework to compute design sensitivities using either the Euler or the Navier–Stokes equations. Once the sensitivity derivatives have been obtained using the adjoint methodology, a quasi-Newton method, referred to as KSOPT (Wrenn, 1989), is used to drive the optimization process.

A test case was devised to test the ability of the optimization method to design an outer wall shape for a channel flow given a target pressure distribution on the lower wall. Subsonic flow ($M = 0.2$) was computed using the Euler equations through a curved channel whose walls are defined by

$$y_{\text{upper}} = \cos[(x+5)/3.18309886] + 0.48, \tag{1}$$

$$y_{\text{lower}} = \cos[(x+5)/3.18309886], \tag{2}$$

and where the walls are straight (horizontal) for $-12 < x < -5$ and for $5 < x < 12$. Then, the outer wall shape was arbitrarily altered as an initial condition and fed into the optimization method along with the lower wall target pressure distribution from the original computation. The shape of the outer wall was parameterized with 36 design variables. The optimization method achieved the desired lower surface pressure distribution (not shown) by solving for the correct outer wall shape, shown in Fig. 1. The maximum error at any grid point from the exact wall shape is less than 1% of the channel width after 20 design cycles.

In the So–Mellor case, the cost function to be minimized is the difference in the pressure distribution on the inner wall from experimental data. The shape of the outer wall is parameterized with 28 design variables. To avoid having to contend with boundary layer separation along the outer wall, the optimization is conducted using the Euler equations and the method is run until the cost function reaches a suitable level of convergence.

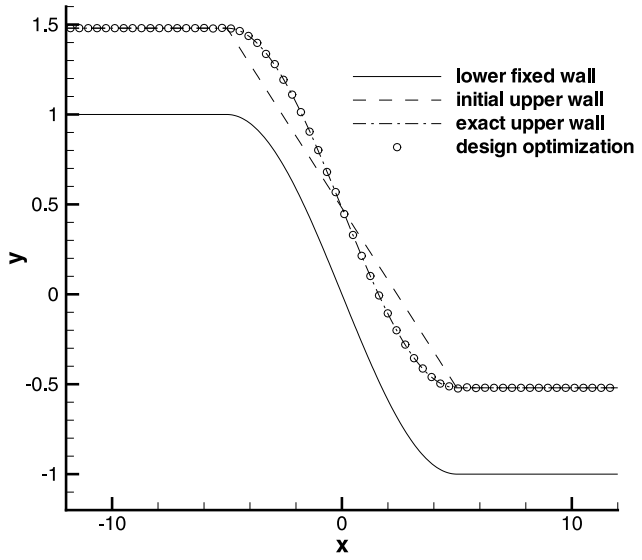

Fig. 1. Wall shape for optimization method test case, with every eighth point of design optimization result shown.

3. Numerical method and turbulence models

The Navier–Stokes CFD code used in the current investigation is CFL3D (Krist et al., 1998), a widely used structured-grid upwind finite-volume method. Details about the code can be found in the User's Manual referenced.

The two turbulence models used are the one-equation SA model (Spalart and Allmaras, 1994) and the two-equation EASM (Rumsey et al., 2000). However, note that the EASM has an additional minor modification, described in Gatski and Rumsey (2001). To summarize, the implicit equation for the Reynolds stress anisotropy tensor in EASM is

$$-(1/a_4)b_{ij} - a_3(b_{ik}S_{kj} + S_{ik}b_{kj} - \tfrac{2}{3}b_{kl}S_{lk}\delta_{ij}) + a_2(b_{ik}W_{kj} - W_{ik}b_{kj}) = a_1 S_{ij}, \tag{3}$$

where $b_{ij} = \tau_{ij}/(2K) - \delta_{ij}/3$, and $K = \tau_{nn}/2$ is the turbulent kinetic energy. The coefficients a_i are given by $a_1 = \frac{1}{2}(\frac{4}{3} - C_2)$, $a_2 = \frac{1}{2}(2 - C_4)$, $a_3 = \frac{1}{2}(2 - C_3)$, and $a_4 = gK/\varepsilon$, where $C_2 = 0.36$, $C_3 = 1.25$, and $C_4 = 0.4$. The modification is in the function g, now given by

$$g = \left[\gamma_0^* \frac{\mathscr{P}}{\varepsilon} + \gamma_1^*\right]^{-1}, \tag{4}$$

where

$$\gamma_0^* = \gamma_0 - 1 \tag{5}$$

and

$$\gamma_1^* = \gamma_1 + 1 + \left(\frac{C_{\varepsilon 2} - C_{\varepsilon 1}}{C_{\varepsilon 1} - 1}\right), \tag{6}$$

and where $\gamma_0 = C_1^1/2 + 1$, $\gamma_1 = C_1^0/2 - 1$, $C_1^0 = 3.4$, $C_1^1 = 1.8$, $C_{\varepsilon 1} = 1.44$, and $C_{\varepsilon 2} = 1.83$.

Gatski and Rumsey (2001) showed that a source of error in the EASM for curved flows was caused by the assumption of anisotropy equilibrium in the Cartesian frame of reference in the derivation of the model directly from the full Reynolds stress model

$$\frac{\mathrm{D}b_{ij}}{\mathrm{D}t} = 0. \tag{7}$$

In the study of non-Newtonian constitutive relations (e.g., Schunk and Scriven, 1990; Souza Mendes et al., 1995), a measure of relative rotation rate is based on the principal axes of the strain rate tensor. By assuming a transformed form of Eq. (7) to hold in this principal axes frame, a new form of the EASM can be derived that takes into account the flow field curvature. This new form is termed EASM curvature-corrected (EASMCC).

In the transformed coordinate frame, the following equation holds:

$$\frac{\mathrm{D}\overline{b}_{ij}}{\mathrm{D}t} = 0, \tag{8}$$

where $\overline{b}_{ij}$ is the transformed anisotropy tensor. Written in the Cartesian frame, Eq. (8) becomes

$$\frac{\mathrm{D}b_{ij}}{\mathrm{D}t} = b_{ik}\,\Omega_{kj} - \Omega_{ik}b_{kj}. \tag{9}$$

The Ω_{ij} tensor is related to the rate of rotation between the principal axes (barred) system and the Cartesian (unbarred) system.

The method for implementation of EASMCC in 2D is as follows. The rotation rate tensor W_{ij} in the model is replaced by an "effective" $W_{ij}^* = W_{ij} - \Omega_{ij}/a_2$, where the constant a_2 is defined by the pressure–strain correlation model. The tensor Ω_{ij} is given by

$$\Omega_{ij} = \begin{bmatrix} 0 & \mathrm{D}\alpha/\mathrm{D}t \\ -\mathrm{D}\alpha/\mathrm{D}t & 0 \end{bmatrix} \tag{10}$$

and $\mathrm{D}\alpha/\mathrm{D}t$ is the Lagrangian derivative of the strain-tensor principal axes, given by

$$\frac{\mathrm{D}\alpha}{\mathrm{D}t} = \frac{\mathrm{D}}{\mathrm{D}t}\left(\tan^{-1}\left[\frac{(S_{11}^2 + S_{12}^2)^{1/2} - S_{11}}{S_{12}}\right]\right). \tag{11}$$

This expression can be reduced to (see Spalart and Shur, 1997)

$$\frac{\mathrm{D}\alpha}{\mathrm{D}t} = \frac{1}{2(S_{11}^2 + S_{12}^2)}\left[S_{11}\frac{\mathrm{D}S_{12}}{\mathrm{D}t} - S_{12}\frac{\mathrm{D}S_{11}}{\mathrm{D}t}\right]. \tag{12}$$

In practice, a term is added to the denominator of Eq. (12) to avoid division by zero as well as to avoid spurious fluctuations in $\mathrm{D}\alpha/\mathrm{D}t$ in regions of very low gradient. Note that for a simple 2D azimuthal flow with only a u_θ component of velocity (a function of radius), the following relation can be derived:

$$\frac{\mathrm{D}\alpha}{\mathrm{D}t} = \frac{1}{2}(S - W)\,\mathrm{sign}(W_{12}), \tag{13}$$

where $S \equiv (2S_{ij}S_{ij})^{1/2}$ and $W \equiv (2W_{ij}W_{ij})^{1/2}$. This analytical function can be shown to hold in general only for $\mathscr{R}^2$ very close to 1, where $\mathscr{R}^2$ is defined by

$$\mathscr{R}^2 \equiv -\frac{\{\mathbf{W}^2\}}{\{\mathbf{S}^2\}} = \frac{W^2}{S^2} \tag{14}$$

and $\{\}$ represents the trace: $\{\mathbf{W}^2\} = W_{ij}W_{ji} = -W_{ij}W_{ij}$ and $\{\mathbf{S}^2\} = S_{ij}S_{ji} = S_{ij}S_{ij}$. Eq. (13) has proved to be useful as a check (in regions where $\mathscr{R}^2 \approx 1$) on the more complicated numerics required to obtain $\mathrm{D}\alpha/\mathrm{D}t$ exactly, but it is of limited use in general. We use the exact $\mathrm{D}\alpha/\mathrm{D}t$ term given by Eq. (12) for all the results in this paper.

A curvature correction for the SA model has been developed by Spalart and Shur (1997), and applied to a variety of flows in Shur et al. (2000). This correction, Spalart–Allmaras for rotation/curvature (SARC) was similarly derived based on the rate of change of the principal axes of the strain rate tensor, but it also includes a heuristic function f_{r1} (that multiplies the model's production term), which is not present in the EASMCC.

Table 1
Wall points (in.) used for So–Mellor case

x_{inner}	y_{inner}	x_{outer}	y_{outer}
0.2400E + 02	0.0000E + 00	0.2400E + 02	0.6000E + 01
0.3350E + 02	0.0000E + 00	0.3406E + 02	0.6000E + 01
0.3580E + 02	0.0000E + 00	0.3668E + 02	0.6004E + 01
0.3780E + 02	0.0000E + 00	0.3905E + 02	0.5983E + 01
0.3957E + 02	0.0000E + 00	0.4119E + 02	0.5969E + 01
0.4116E + 02	0.0000E + 00	0.4315E + 02	0.5954E + 01
0.4258E + 02	0.0000E + 00	0.4495E + 02	0.5958E + 01
0.4388E + 02	0.0000E + 00	0.4661E + 02	0.5978E + 01
0.4506E + 02	0.0000E + 00	0.4815E + 02	0.6171E + 01
0.4615E + 02	0.0000E + 00	0.4957E + 02	0.6390E + 01
0.4716E + 02	0.1652E − 02	0.5092E + 02	0.6508E + 01
0.4810E + 02	−0.5451E − 02	0.5220E + 02	0.6466E + 01
0.4898E + 02	−0.6397E − 01	0.5339E + 02	0.6254E + 01
0.4980E + 02	−0.1668E + 00	0.5448E + 02	0.5904E + 01
0.5057E + 02	−0.3273E + 00	0.5548E + 02	0.5456E + 01
0.5128E + 02	−0.5392E + 00	0.5639E + 02	0.4941E + 01
0.5194E + 02	−0.7944E + 00	0.5723E + 02	0.4379E + 01
0.5255E + 02	−0.1081E + 01	0.5799E + 02	0.3784E + 01
0.5313E + 02	−0.1391E + 01	0.5870E + 02	0.3165E + 01
0.5366E + 02	−0.1721E + 01	0.5935E + 02	0.2530E + 01
0.5416E + 02	−0.2067E + 01	0.5995E + 02	0.1886E + 01
0.5462E + 02	−0.2428E + 01	0.6051E + 02	0.1236E + 01
0.5506E + 02	−0.2802E + 01	0.6104E + 02	0.5848E + 00
0.5546E + 02	−0.3189E + 01	0.6155E + 02	−0.6808E − 01
0.5584E + 02	−0.3588E + 01	0.6202E + 02	−0.7222E + 00
0.5619E + 02	−0.3999E + 01	0.6248E + 02	−0.1379E + 01
0.5651E + 02	−0.4419E + 01	0.6290E + 02	−0.2040E + 01
0.5682E + 02	−0.4849E + 01	0.6331E + 02	−0.2707E + 01
0.5710E + 02	−0.5288E + 01	0.6369E + 02	−0.3382E + 01
0.5736E + 02	−0.5737E + 01	0.6404E + 02	−0.4069E + 01
0.5759E + 02	−0.6195E + 01	0.6435E + 02	−0.4768E + 01
0.5781E + 02	−0.6663E + 01	0.6464E + 02	−0.5480E + 01
0.5801E + 02	−0.7142E + 01	0.6489E + 02	−0.6209E + 01
0.5819E + 02	−0.7631E + 01	0.6510E + 02	−0.6953E + 01
0.5835E + 02	−0.8133E + 01	0.6528E + 02	−0.7713E + 01
0.5848E + 02	−0.8646E + 01	0.6541E + 02	−0.8490E + 01
0.5860E + 02	−0.9173E + 01	0.6550E + 02	−0.9282E + 01
0.5869E + 02	−0.9714E + 01	0.6554E + 02	−0.1009E + 02
0.5876E + 02	−0.1027E + 02	0.6554E + 02	−0.1091E + 02
0.5880E + 02	−0.1084E + 02	0.6550E + 02	−0.1175E + 02
0.5881E + 02	−0.1143E + 02	0.6542E + 02	−0.1261E + 02
0.5880E + 02	−0.1204E + 02	0.6530E + 02	−0.1348E + 02
0.5876E + 02	−0.1266E + 02	0.6514E + 02	−0.1438E + 02
0.5868E + 02	−0.1331E + 02	0.6495E + 02	−0.1529E + 02
0.5856E + 02	−0.1398E + 02	0.6471E + 02	−0.1623E + 02
0.5840E + 02	−0.1467E + 02	0.6443E + 02	−0.1720E + 02
0.5819E + 02	−0.1538E + 02	0.6411E + 02	−0.1820E + 02
0.5793E + 02	−0.1612E + 02	0.6373E + 02	−0.1923E + 02
0.5760E + 02	−0.1688E + 02	0.6327E + 02	−0.2028E + 02
0.5719E + 02	−0.1766E + 02	0.6273E + 02	−0.2136E + 02
0.5671E + 02	−0.1847E + 02	0.6208E + 02	−0.2246E + 02
0.5613E + 02	−0.1929E + 02	0.6129E + 02	−0.2356E + 02
0.5544E + 02	−0.2014E + 02	0.6033E + 02	−0.2464E + 02
0.5462E + 02	−0.2099E + 02	0.5918E + 02	−0.2567E + 02
0.5363E + 02	−0.2182E + 02	0.5782E + 02	−0.2663E + 02
0.5246E + 02	−0.2263E + 02	0.5627E + 02	−0.2756E + 02
0.5110E + 02	−0.2345E + 02	0.5454E + 02	−0.2846E + 02
0.4957E + 02	−0.2433E + 02	0.5263E + 02	−0.2944E + 02
0.4783E + 02	−0.2533E + 02	0.5055E + 02	−0.3056E + 02
0.4584E + 02	−0.2647E + 02	0.4826E + 02	−0.3185E + 02
0.4354E + 02	−0.2780E + 02	0.4572E + 02	−0.3332E + 02
0.4084E + 02	−0.2935E + 02	0.4288E + 02	−0.3505E + 02
0.3761E + 02	−0.3122E + 02	0.3962E + 02	−0.3699E + 02

In the SA model, a portion of the production term is given by the expression $P = c_{b1}[1 - f_{t2}]W\tilde{v}$. In the current implementation of the SARC model, P is replaced by $P' = c_{b1}[f_{r1} - f_{t2}]W\tilde{v}$, where

$$f_{r1} = (1 + c_{r1})\frac{2r^*}{(1 + r^*)}[1 - c_{r3}\tan^{-1}(c_{r2}\tilde{r})] - c_{r1} \tag{15}$$

and $c_{r1} = 1$, $c_{r2} = 12$. The constant c_{r3} has been assigned to be both 1.0 and 0.6 in Spalart and Shur (1997) (Spalart and Shur suggest that they are still experimenting with the function f_{r1}). In the current study, we use both values, and show that $c_{r3} = 0.6$ is the more appropriate choice for this case. The function r^* is given by $r^* \equiv S/W$. It is related to the flow parameter defined in Eq. (14). The $\tilde{r}$ term is computed using

$$\tilde{r} = 2W_{ik}S_{jk}\left[\frac{\mathrm{D}S_{ij}}{\mathrm{D}t} + (\epsilon_{imn}S_{jn} + \epsilon_{jmn}S_{in})\omega_m\right]\Big/ D^4, \tag{16}$$

where the ω_m term represents the system rotation and $D \equiv [\frac{1}{2}(S^2 + W^2)]^{1/2}$. For 2D flows and no system rotation, the expression for $\tilde{r}$ reduces to

$$\tilde{r} = -\left(\frac{\mathrm{D}\alpha}{\mathrm{D}t}\right)\frac{8W_{12}(S_{11}^2 + S_{12}^2)}{D^4}, \tag{17}$$

with $\mathrm{D}\alpha/\mathrm{D}t$ given by Eq. (12).

4. Results

In the So–Mellor experiment, the curved wall tunnel had an aspect ratio of 8 (depth of 48 in.) and the flow along the tunnel centerline was nominally 2D. Thus, 2D computations are expected to adequately represent the flow field. The inner wall shape is defined by a series of nine arc segments of varying angle and radius. The initial radius of curvature is 10 in., and the final radius of curvature is 13.86 in. The curved wall turns through a total of 150°. A detailed description of the inner wall shape can be found in So and Mellor (1973). The channel width is 6 in. at the inlet. An outer wall shape was obtained from the optimization program, which was run in Euler mode to obtain a shape such that the inner wall pressure distribution matched experiment throughout most of the curved region. A list of resulting outer wall points is given in Table 1 (only 63 points are given, for brevity). Inner wall points are given also, for reference.

The grid employed in the Navier–Stokes computations is shown in Fig. 2. The grid size is 257×161, with a minimum normal spacing at the convex wall of 0.00015 in. This corresponds with a wall variable spacing of approximately $y^+ = 0.3$. The grid extends from 24 in. upstream of the curved wall to approximately 18 in. downstream of the end of curvature. The Reynolds number per inch is taken as 3.6417×10^4, and the nominal Mach number at the inlet is $M = 0.063$. At the inflow boundary, the u-velocity profile is set based on the experimentally measured skin friction and boundary layer thickness. The turbulence quantities are set to match the experimental levels at the same location. At the outflow boundary, pressure is specified at $p/p_{\mathrm{ref}} = 1$, and all other quantities are extrapolated from the interior of the grid. Additional details concerning the boundary condition specifications can be found in Rumsey et al. (2000).

Slip-wall boundary conditions are applied at the outer wall in the CFD simulation. This boundary condition is consistent with the assumption used in the optimization method, and allows the simulation to be run without the complication of having to contend with tangential jet or bleed boundary conditions. At the inner wall, standard no-slip adiabatic solid wall boundary conditions are employed.

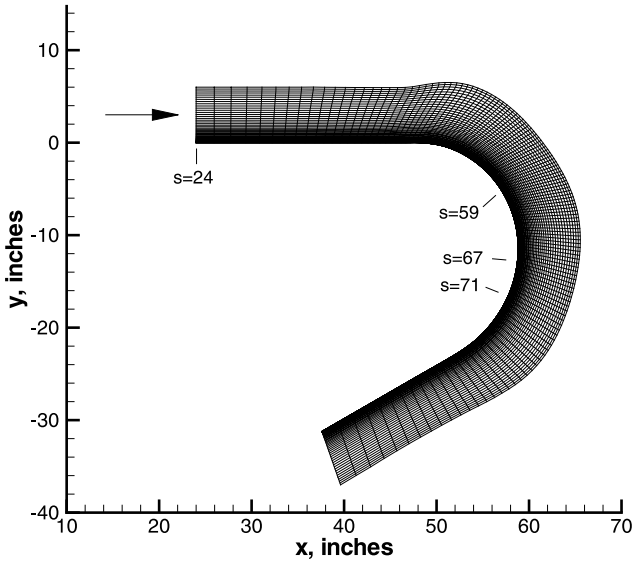

Fig. 2. Grid for So–Mellor case, every other point of 257×161 grid shown.

For the remainder of the paper, we adopt a coordinate system with s measured along the inner wall in the flow direction and d measured normal to the inner wall. Thus, s represents the surface coordinates, or length measured along the inner wall surface. The boundary layer thickness at the inflow ($s = 24$ in.) is approximately 0.55 in., whereas at the start of the curvature ($s = 48$ in.) it is approximately 0.95 in. Thus, at the start of curvature, the parameter δ/R is roughly 0.095. According to Patel and Sotiropoulos (1997), $\delta/R < 0.01$ represents very mild curvature, whereas $0.1 < \delta/R < 1$ represents moderate to strong curvature. Therefore, the curvature for this case can probably be categorized as "moderate", whereas the Monson and Seegmiller U-duct case (with $\delta/R = 0.5$) can be categorized as "strong" (see Monson and Seegmiller, 1992; Rumsey et al., 2000).

In the experiment, the outer wall shape was set to allow a small pressure drop near the start of curvature, followed by a region of nearly constant pressure all the way to the end of the curved surface, at $s = 79.43$ in. Surface pressure coefficients are shown in Fig. 3 using two different turbulence models. The pressures match experiment very well over most of the inlet and curved wall segments. The small differences upstream of the start of curvature are likely due to the fact that CFD uses a slip-wall boundary condition at the outer wall and does not model the local tangential jet in the experiment.

The effect of grid density on a typical solution is shown in Figs. 4 and 5. In these figures, the "fine" level is the 257×161 grid, "medium" has every other grid point removed in both directions, and "coarse" has every other grid point removed again. For this flow, the skin friction shows about a 3–5% difference between the coarse grid and fine grid solutions in the curved region, and roughly 1% difference (or less) between results on the medium and fine grids. The turbulent shear stress shows almost no difference between any of the grid levels. For all the remaining results in the paper, the medium level grid is employed.

The effect of the SARC model constant c_{r3} is shown in Fig. 6. Note that the c_f levels are referenced to the nominal velocity at the inlet, rather than the local "potential flow velocity at the wall", as reported in So and Mellor (1973). The experimental levels have been adjusted accordingly. The original SA model yields high c_f levels over most of the curved wall region. When

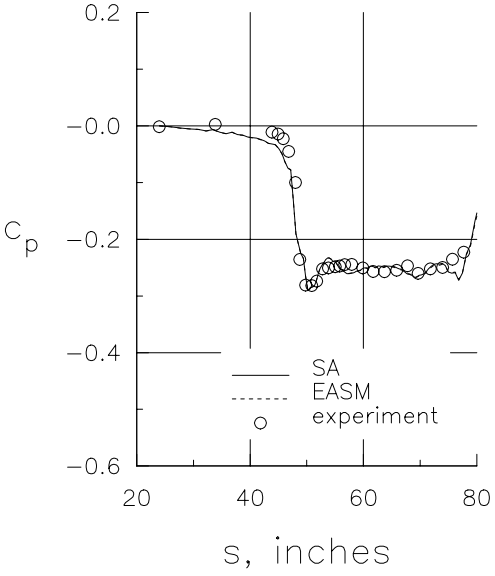

Fig. 3. Surface pressure coefficient, referenced to inlet conditions.

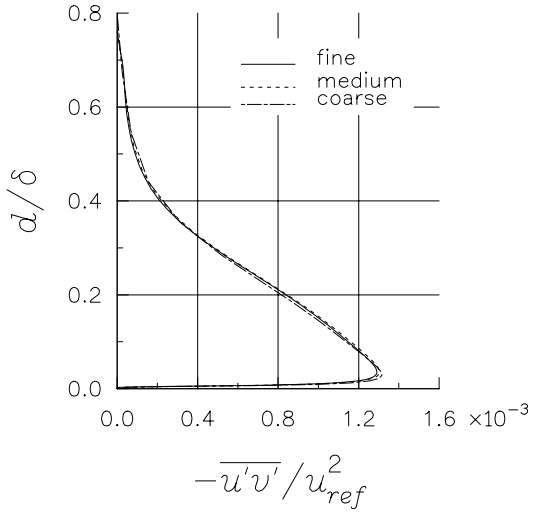

Fig. 5. Effect of grid size on turbulent shear stress profile at $s = 71$ in., EASMCC.

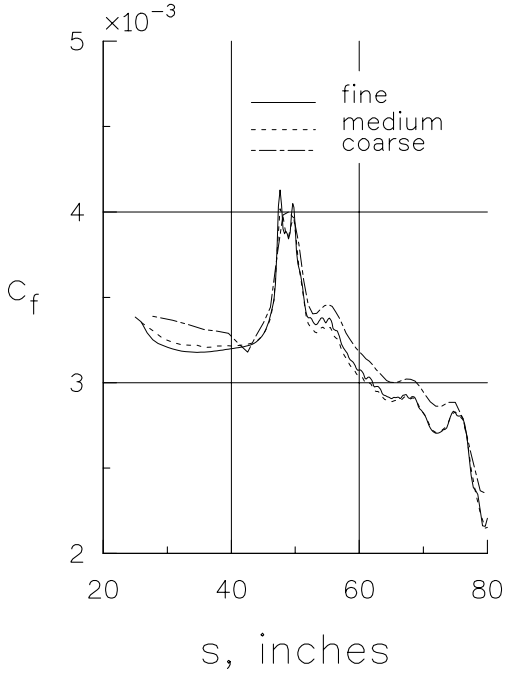

Fig. 4. Effect of grid size on surface skin friction coefficient, EASMCC.

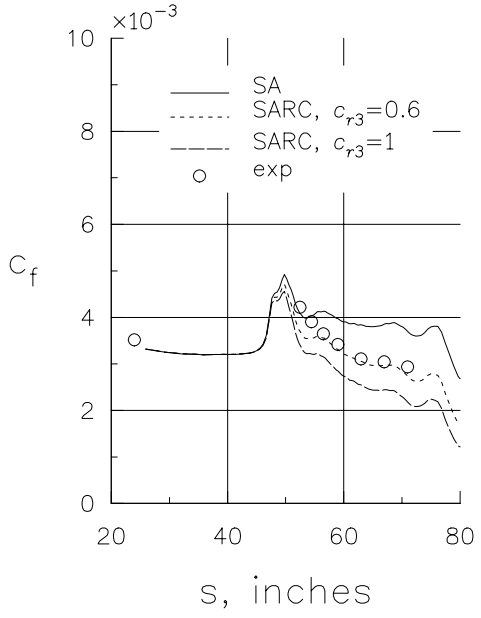

Fig. 6. Effect of SARC model constant on surface skin friction coefficient, referenced to inlet conditions.

SARC with $c_{r3} = 0.6$ is used, c_f levels agree well with experiment, but SARC with $c_{r3} = 1.0$ predicts c_f levels that are too low. Unless otherwise noted, for all remaining SARC results, a value for the constant $c_{r3} = 0.6$ is used.

Surface skin friction results using all four versions of the turbulence models are shown in Fig. 7. EASM and EASMCC are both low near the beginning of curvature but are relatively close to experimental levels over much of the curved wall region beyond $s \approx 55$ in.; EASMCC reduces the c_f levels from that of EASM by only a modest amount. Overall, SARC, EASM, and EASMCC produce similar c_f levels over most of the curved region in reasonable agreement with experiment.

Velocity profiles in the bend are plotted in Fig. 8. In addition to results in the curved region, profiles are shown at the inlet ($s = 24$ in. station), although experimental data are not available at this location. As mentioned earlier, the velocity profile is set at the inflow to match the experimental c_f, δ, and nominal velocity using law-of-the-wall relations. As seen in the figure, initial profiles at the inlet are essentially identical for all four models. In the curved region, the results begin to differ. The three models SARC, EASM, and EASMCC are very close to each other and are in good agreement with experiment. However, the SA model predicts higher velocity levels over the first 20% of the boundary layer at all three stations.

Turbulent shear stress profiles are plotted in Fig. 9 for SA and SARC and in Fig. 10 for EASM and EASMCC. All shear and normal stress profiles, to be given below, are in the local

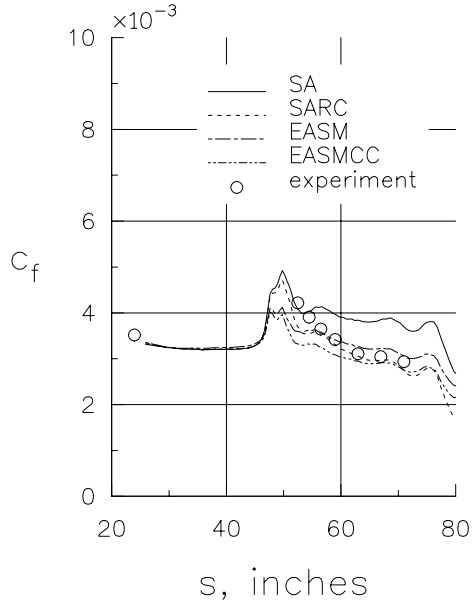

Fig. 7. Surface skin friction coefficient, referenced to inlet conditions.

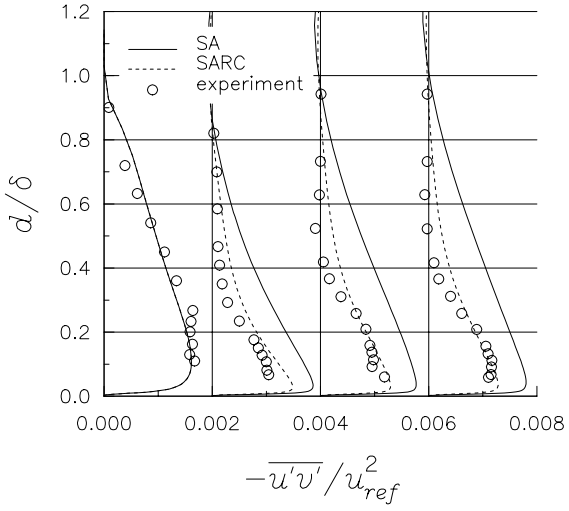

Fig. 9. Turbulent shear stress profiles for the SA and SARC models at $s = 24$ in., $s = 59$ in., $s = 67$ in., and $s = 71$ in., referenced to inlet conditions (origin for each successive station is shifted 0.002 units to the right).

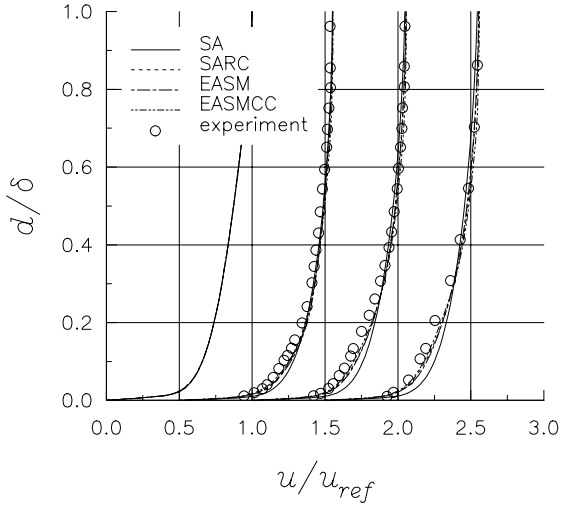

Fig. 8. Velocity profiles at $s = 24$ in., $s = 59$ in., $s = 67$ in., and $s = 71$ in., referenced to inlet conditions (origin for each successive station is shifted 0.5 units to the right).

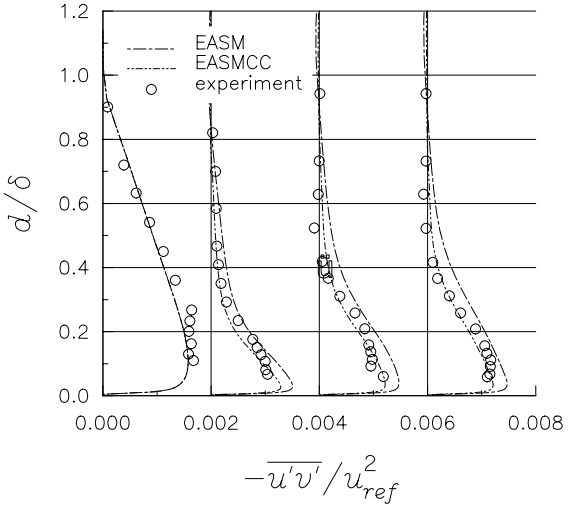

Fig. 10. Turbulent shear stress profiles for the EASM and EASMCC at $s = 24$ in., $s = 59$ in., $s = 67$ in., and $s = 71$ in., referenced to inlet conditions (origin for each successive station is shifted 0.002 units to the right).

body/normal coordinate system. Stresses in this frame are related to those in the Cartesian frame by the following relations:

$$\overline{u'v'} = \tfrac{1}{2}(\overline{v'v'}_c - \overline{u'u'}_c)\sin(2\Theta) + \overline{u'v'}_c\cos(2\Theta), \tag{18}$$

$$\overline{u'u'} = \overline{u'u'}_c\cos^2\Theta + \overline{v'v'}_c\sin^2\Theta + \overline{u'v'}_c\sin(2\Theta), \tag{19}$$

$$\overline{v'v'} = \overline{v'v'}_c\cos^2\Theta + \overline{u'u'}_c\sin^2\Theta - \overline{u'v'}_c\sin(2\Theta), \tag{20}$$

where the subscript c indicates Cartesian frame, and Θ is the angle that the body tangent vector makes with the x-axis. In Fig. 9, the SA model significantly overpredicts the $-\overline{u'v'}$ levels in the curved region, whereas SARC agrees much better with experiment. The differences between EASM and EASMCC in Fig. 10 are much less marked. However, EASMCC is generally in better agreement with experiment, particularly for $d/\delta > 0.3$, where the turbulence is suppressed to near-zero levels.

The turbulent normal stresses are plotted for EASM and EASMCC in Figs. 11 and 12. Because EASM and EASMCC are non-linear models, they can predict the normal stress differences between $\overline{u'u'}$ and $\overline{v'v'}$. Results are in good agreement with experiment at the inflow and throughout the curvature region. The curvature correction in EASMCC has the effect of lowering the normal stress levels slightly from those of EASM. The $\overline{u'u'}$ and $\overline{v'v'}$ for SA and SARC are not shown. Linear eddy viscosity models cannot predict the normal stress differences, although the ability to predict these differences is generally not considered necessary for most thin shear flow applications.

Finally, the velocity profiles are shown using wall variables in Figs. 13–15. The theoretical log-law curve plotted in these figures is due to Spalding (White, 1974). In the experimental results of Fig. 13, it is noted that the effect of curvature is

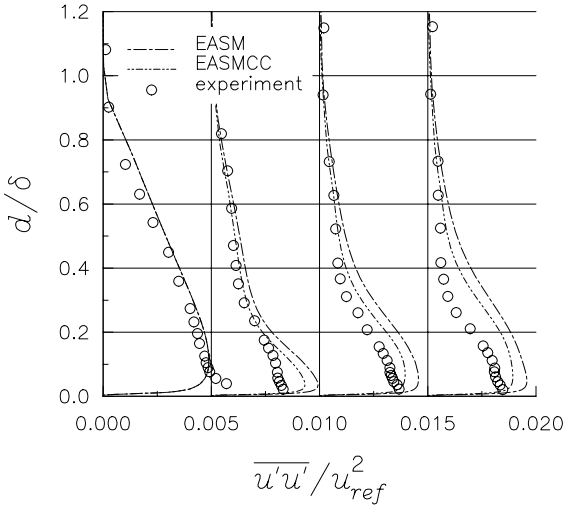

Fig. 11. $\overline{u'u'}$ turbulent normal stress profiles for the EASM and EASMCC at $s = 24$ in., $s = 59$ in., $s = 67$ in., and $s = 71$ in., referenced to inlet conditions (origin for each successive station is shifted 0.005 units to the right).

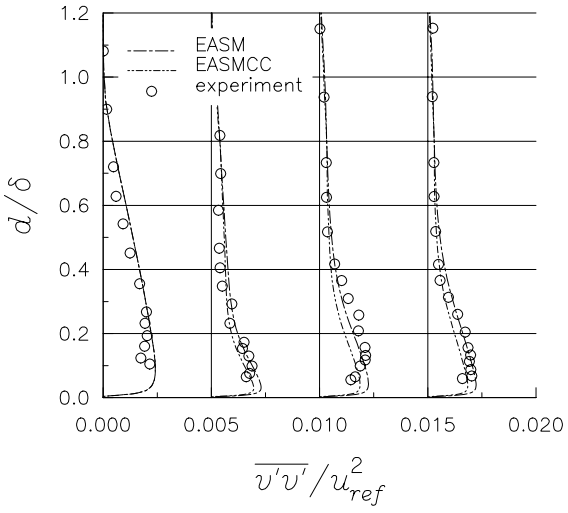

Fig. 12. $\overline{v'v'}$ turbulent normal stress profiles for the EASM and EASMCC at $s = 24$ in., $s = 59$ in., $s = 67$ in., and $s = 71$ in., referenced to inlet conditions (origin for each successive station is shifted 0.005 units to the right).

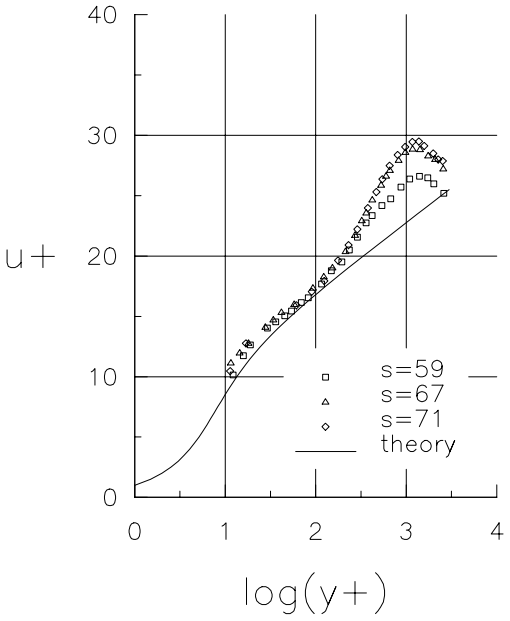

Fig. 13. Experimental velocity profiles using wall variables.

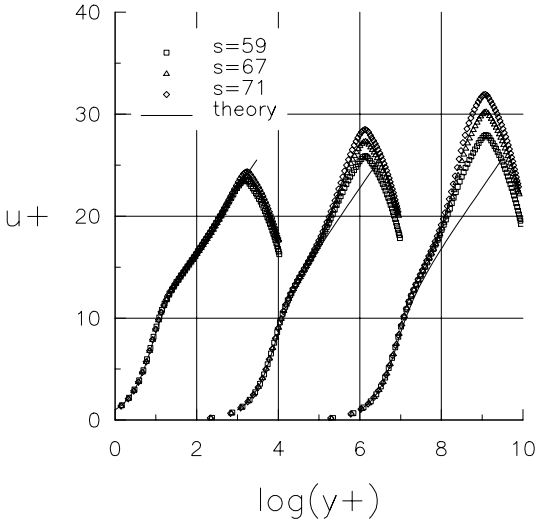

Fig. 14. Velocity profiles using wall variables for SA and SARC (SARC with $c_{r3} = 0.6$ is shifted 3 units to the right, and SARC with $c_{r3} = 1.0$ is shifted 6 units to the right).

primarily in the wake region beyond the log layer, where the u^+ levels are increased at successive stations downstream. The log layer itself remains unaffected by curvature. The SARC model overall reflects the correct trend, increasing u^+ in the wake region with downstream distance in the curve. However, the effect is excessive when $c_{r3} = 1.0$, and even the log layer itself is affected by the curvature correction and loses the correct slope. When $c_{r3} = 0.6$, a portion of the log layer retains the correct slope and only the region beyond $y^+ \approx 100$ is altered. In Fig. 15, the EASMCC shows somewhat elevated wake levels of u^+, similar in character to the experiment, even with no curvature correction. These levels are raised slightly through the use of the curvature correction in EASMCC. In both EASM and EASMCC, the log layer remains in good agreement with the theoretical slope.

It is also instructive to return to check the original assumption made in the derivation of the EASMCC. We already know from previous studies (e.g., Rumsey et al., 2000) that the assumption Eq. (7) is not valid in regions of high curvature. We would now like to investigate the validity of the transformed equation, Eq. (9). We do this by computing its actual value (the quantity $u_j \partial b_{ik}/\partial x_j$) at various locations in the converged solution, and comparing it to the quantity $b_{ik}\Omega_{kj} - \Omega_{ik}b_{kj}$.

Results are shown in Figs. 16 and 17 for Db_{11}/Dt and Db_{12}/Dt, respectively. The three successive curves in each figure represent results at the three stations in the curved region. It is shown in these figures that the assumption Eq. (9) is indeed valid in the curvature region, and is nearly exact in the lower part of the boundary layer.

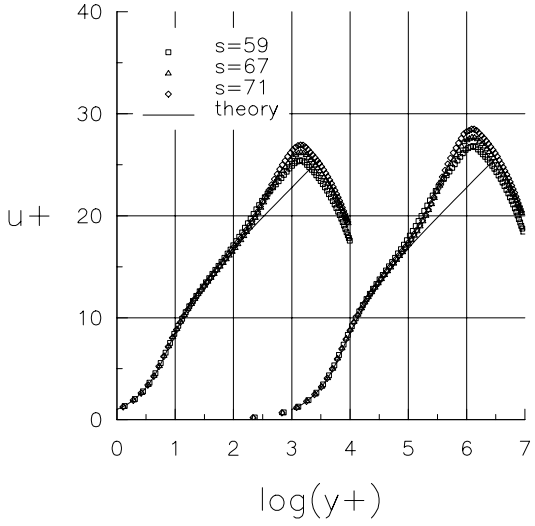

Fig. 15. Velocity profiles using wall variables for EASM and EASMCC (EASMCC is shifted 3 units to the right).

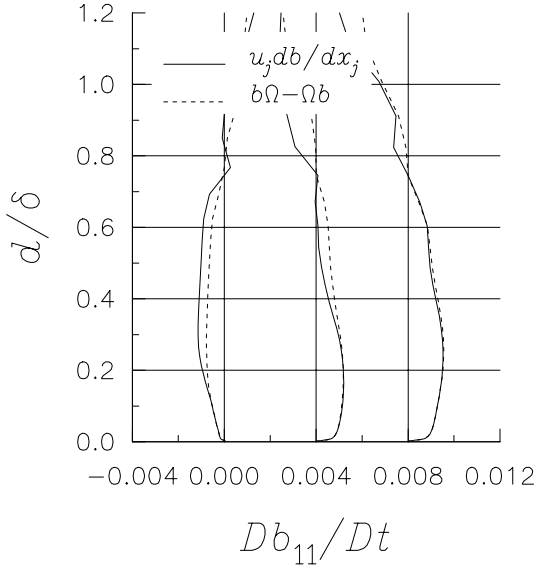

Fig. 16. Comparison of actual Db_{11}/Dt with EASMCC assumption at $s = 59$ in., $s = 67$ in., and $s = 71$ in. (origin for each successive station is shifted 0.004 units to the right).

5. Conclusions

An adjoint optimization method was shown to be useful in determining an outer wall shape for a zero pressure gradient curved duct flow, given the target inner wall pressure distribution. This procedure, easily generalizable to other configurations, extended the usefulness of the So–Mellor data base to Navier–Stokes CFD codes. As a result, a unique evaluation of turbulence models for predicting curvature effects was made.

The numerical study yielded the following conclusions. Of the models studied, the standard SA model (with no curvature correction) did the poorest job modeling the flow field with convex curvature. Eddy viscosity levels were significantly overpredicted, and velocity profiles were somewhat too full. The skin friction coefficient in the curved region was over-

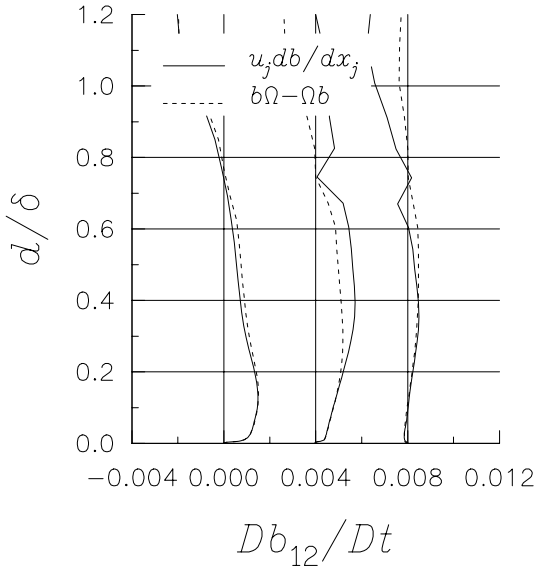

Fig. 17. Comparison of actual Db_{12}/Dt with EASMCC assumption at $s = 59$ in., $s = 67$ in., and $s = 71$ in. (origin for each successive station is shifted 0.004 units to the right).

predicted. The curvature correction in SARC significantly improved results, lowering eddy viscosity levels and bringing velocity profiles into better agreement with experiment. The best choice for the model constant c_{r3} was 0.6 for this test case. A value of $c_{r3} = 1.0$ lowered the skin friction coefficient too much, and the log layers of the velocity profiles were significantly altered.

EASM and EASMCC both did a good job predicting this flow field. EASMCC was derived by assuming anisotropy equilibrium in the reference frame defined by the principal axes of the strain rate tensor, rather than in the Cartesian frame for standard EASM. Unlike SARC, no heuristic functions and no additional constants were necessary in EASMCC. The modified assumption on the anisotropy tensor was shown to be valid in the curved region of the flow field. The resulting curvature correction in EASMCC had only a minor effect for this case compared to EASM, slightly lowering the turbulent stress levels (in better agreement with experiment) and lowering the skin friction coefficient by a small amount. The effect on computed velocity profiles was minimal.

Therefore it appeared that some aspect of the EASM enabled it to perform reasonably well for this curved-flow case even without a curvature correction. Because the EASM was derived directly from the Reynolds stress model, it retained some of the invariance properties of the full differential form, even with the incorrect $Db_{ij}/Dt = 0$ assumption. Thus EASM yielded a better physical representation of the turbulence than the lower-order SA model. By including the curvature correction (in EASMCC), *all* the frame-invariance properties were retained. This modification did improve certain details in this flow field, but overall the effects were relatively minor.

Acknowledgements

The first author also wishes to thank P.R. Spalart of the Boeing Company and M.K. Strelets of the Federal Scientific Center of Applied Chemistry (Russia) for their assistance and helpful discussions.

References

Anderson, W.K., Bonhaus, D.L., 1999. Airfoil design on unstructured grids for turbulent flows. AIAA J. 37 (2), 185–191.

Gatski, T.B., Rumsey, C.L., 2001. Linear and non-linear eddy viscosity models. In: B.E. Launder, N.D. Sandham (Eds.), Closure Strategies for Turbulent and Transitional Flows, Cambridge University Press, Cambridge, p. 9–46.

Gatski, T.B., Speziale, C.G., 1993. On explicit algebraic stress models for complex turbulent flows. J. Fluid Mech. 254, 59–78.

Gillis, J.C., Johnston, J.P., 1983. Turbulent boundary-layer flow and structure on a convex wall and its redevelopment on a flat wall. J. Fluid Mech. 135, 123–153.

Krist, S.L., Biedron, R.T., Rumsey, C.L., 1998. CFL3D User's Manual (version 5.0), NASA TM-1998-208444.

Menter, F.R., 1994. Two-equation eddy-viscosity turbulence models for engineering applications. AIAA J. 32 (8), 1598–1605.

Monson, D.J., Seegmiller, H.L., 1992. An experimental investigation of subsonic flow in a two-dimensional U-duct, NASA TM 103931.

Nielsen, E.J., Anderson, W.K., 1999. Aerodynamic design optimization on unstructured meshes using the Navier–Stokes equations. AIAA J. 37 (11), 1411–1419.

Nielsen, E.J., Anderson, W.K., 2001. Recent improvements in aerodynamic design optimization on unstructured meshes. AIAA Paper 2001-0596, Reno, NV.

Patel, V.C., Sotiropoulos, F., 1997. Longitudinal curvature effects in turbulent boundary layers. Prog. Aerospace Sci. 33, 1–70.

Rumsey, C.L., Gatski, T.B., Morrison, J.H., 2000. Turbulence model predictions of strongly-curved flow in a U-duct. AIAA J. 38 (8), 1394–1402.

Schunk, P.R., Scriven, L.E., 1990. Constitutive equation for modeling mixed extension and shear in polymer solution processing. J. Rheol. 34, 1085–1119.

Shur, M., Strelets, M., Travin, A., Spalart, P.R., 2000. Turbulence modeling in rotating and curved channels: assessing the Spalart–Shur correction. AIAA J. 38 (5), 784–792.

So, R.M.C., Mellor, G.L., 1973. Experiment on convex curvature effects in turbulent boundary layers. J. Fluid Mech. 60 (Part 1), 43–62.

Souza Mendes, P.R., Padmanabhan, M., Scriven, L.E., Macosko, C.W., 1995. Inelastic constitutive equations for complex flows. Rheol. Acta 34, 209–214.

Spalart, P.R., Allmaras, S.R., 1994. A one-equation turbulence model for aerodynamic flows. La Recherche Aerospatiale 1, 5–21.

Spalart, P.R., Shur, M., 1997. On the sensitization of turbulence models to rotation and curvature. Aerospace Sci. Technol. 5, 297–302.

White, F.M., 1974. In: Viscous Fluid Flow. McGraw-Hill, New York, pp. 475–476.

Wilcox, D.W., 1998. In: Turbulence Modeling For CFD. DCW Industries, La Canada, pp. 274–280.

Wrenn, G.A., 1989. An indirect method for numerical optimization using the Kresselmeier–Steinhauser function, NASA CR-4220.